

# Dual ionic gate transistor: a device to induce extreme electric fields in 2D materials

Benjamin I. Weintrub<sup>1</sup>, Yu-Ling Hsieh<sup>12</sup>, Jan N. Kirchhof<sup>1</sup>, and Kirill I. Bolotin<sup>\*1</sup>

1. Department of Physics, Freie Universität Berlin, Berlin, Germany
2. Department of Mechanical Engineering, National Central University, Taoyuan City, Taiwan

## Abstract

We demonstrate a new type of dual gate transistor to induce record electric fields through two-dimensional materials (2DMs). At the heart of this device is a 2DM suspended between two volumes of ionic liquid (IL) with independently controlled potentials. The potential difference between the ILs falls across an ultrathin layer consisting of the 2DM and the electrical double layers above and below it, thereby producing an intense electric field across the 2DM. We determine the field strength via i) direct measurements of electrochemical potentials of the ILs and ii) electrical transport measurements of a semiconducting 2DM, bilayer WSe<sub>2</sub>. The field strength across the material reaches  $\sim 3$  V/nm, the largest static electric field through any electronic device to date. We demonstrate that this field is strong enough to close the bandgap of bilayer WSe<sub>2</sub> driving a semiconductor-to-metal transition. Our approach grants access to previously-inaccessible phenomena occurring in ultrastrong electric fields.

## Introduction

Electric fields are widely used to control material properties and to explore new and diverse physical phenomena. The first group of phenomena appears due to changes of the carrier density induced in a material by the field at its surface, typically explored using field-effect transistors (FETs)<sup>1,2</sup>. Electric fields also cause a second, qualitatively different, group of effects when the field penetrates through the material's bulk. In this case, the presence of a field inside the material breaks symmetries<sup>3-7</sup>, bends the band structure along the direction of the field<sup>3,5-7</sup>, and modifies the energetics of excitons with a dipole moment parallel to the field<sup>3-6,8,9</sup>. In conventional FETs, the induced carriers at the material's surface almost completely screen the field in the bulk of the material. Therefore, a dual gate FET with a pair of gate electrodes above and below the material under study is used to explore the effects of an external electric field penetrating a material. In this configuration, the field strength is controlled by the potential difference between the bottom and top gates, while the Fermi level is determined by their sum<sup>5,7-9</sup>. However, an important limitation for studying large electric fields in conventional solid-state FETs is the breakdown of gate dielectrics happening at around  $0.5 - 1.0$  V/nm<sup>10-16</sup> (somewhat larger dielectric strengths are measured using local probe techniques<sup>11,12</sup>).

The limitation on the maximum achievable carrier density has been overcome during the last decade via ionic gating, the approach that revolutionized condensed matter physics by combining it with electrochemistry<sup>17,18</sup>. In that technique, an ionic compound such as ionic liquid (IL), a molten salt consisting of anions and cations, is placed over a material under study<sup>17-20</sup>. A potential applied between the gate electrode inside the liquid and the sample falls

predominantly over an atomically thick ( $\leq 1$  nm) electric double layer (EDL) at the IL/sample interface, modeled as a capacitor with an exceptionally large geometric areal capacitance ( $\sim 1 \mu\text{F}/\text{cm}^2$ )<sup>17,19,21–26</sup>. The resulting electric field inside the EDL induces a carrier density inside the material<sup>27</sup>. Critically, the field generated here is not limited by the dielectric breakdown of gate dielectrics which limit the performance of conventional solid-state FETs. Instead, the only significant limitation is electrochemical modification of the material or electrodes, which occurs when the potential drop across a particular interface is too large (outside the electrochemical window)<sup>28</sup>. Ionic gating enabled previously inaccessible carrier densities  $>10^{14} \text{ cm}^{-2}$  to be reached<sup>19,27,29,30</sup>. The interactions between electrons at these carrier densities result in structural phase transitions<sup>31</sup> and new electronic phases such as exotic superconductivity<sup>29,30</sup> and gate-controlled ferromagnetism<sup>32</sup>. These effects are especially pronounced in 2DMs such as graphene, transition metal dichalcogenides (TMDCs), or phosphorene, where the carriers are spatially confined to one or few atomic layers<sup>18</sup>.

Despite the progress in using ionic gating to induce high carrier densities, the approach has not been used to generate intense external electric fields inside the bulk of materials. Although hybrid approaches have been used<sup>33–36</sup>, no ionic counterpart to dual gate FETs has been demonstrated. Because of that, a wide range of phenomena predicted to emerge at fields stronger than  $F_{\perp} \sim 1 \text{ V/nm}$  remains inaccessible in solid state devices. For example, for fields near  $F_{\perp} \sim 2 - 3 \text{ V/nm}$ , the interlayer bandgap of bilayer (2L) TMDCs is expected to decrease to zero<sup>37,38</sup>. In this situation, interlayer excitons should start forming at zero energy costs and a transition into a new state of matter, an interlayer excitonic insulator<sup>39</sup>, may occur. Other predicted yet unobserved phenomena at extreme fields include an insulator to topological insulator transition in phosphorene ( $F_{\perp} > 3 \text{ V/nm}$ )<sup>40</sup>, topological insulator to semimetal to normal insulator transition in 1T' TMDCs ( $F_{\perp} > 2 \text{ V/nm}$ )<sup>41</sup>, and structural change in chirality for monolayer Te ( $F_{\perp} > 7 \text{ V/nm}$ )<sup>42</sup>.

Here, we develop a double-sided ionic gating approach to generate ultrastrong electric fields. The approach can be viewed as a counterpart to conventional dual gated FETs which is not limited by the breakdown of gate dielectrics. To generate the field inside a 2DM, we apply a potential difference between the two ILs above and below the 2DM, thereby generating a new type of EDL consisting of two ILs separated by an ultrathin membrane. We use a combination of electrochemical and electrical transport measurements to record an electric field of  $\sim 3 \text{ V/nm}$  inside 2DMs, at least three times higher than the biggest fields reported for conventional solid-state FET technologies.

## Device concept

At the core of our approach to generate and measure large perpendicular electric fields is an electrically-contacted 2DM suspended between two volumes of IL (Fig. 1a). The potential difference between the top and bottom ILs,  $\Delta V^{\text{ref}}$ , is controlled by separate top and bottom gate electrodes in contact with their respective ILs. That potential difference falls across an ultrathin capacitor consisting of the 2DM (thickness  $d_{2\text{DM}} \approx 0.6 \text{ nm}$  for 1L TMDCs) and two EDLs (average

thickness  $d_{\text{EDL}} \approx 0.6$  nm), one above and one below the 2DM<sup>21–26</sup>. Neglecting the variation in the dielectric constant at the nanometer scale, we estimate the field inside that layer as  $F_{\perp} = \Delta V^{\text{ref}}/d_{\text{ion}}$ , where  $d_{\text{ion}} = d_{\text{2DM}} + 2d_{\text{EDL}}$  is the layer thickness. Approximating  $\Delta V^{\text{ref}} \approx 6$  V (corresponding to the potential of top and bottom ILs at  $\pm 3$  V, the electrochemical window of our IL), we can estimate an achievable field strength of  $\sim 3$  V/nm for our 1L devices, at least three times larger than what is possible for dielectric-based devices.

We determine the field strength using a specific 2DM, bilayer WSe<sub>2</sub>, as a field sensor. We use electrical transport measurements to determine the bandgap of the 2DM<sup>19</sup>, which is known to exhibit a strong dependence on perpendicular electric fields<sup>9,37,38</sup>. When no field is present, the band structure of 2L WSe<sub>2</sub> can be approximated as a pair of energy-degenerate conduction and valence bands corresponding to top and bottom TMDC layers. An external perpendicular electric field breaks the inversion symmetry of the bilayer, thereby inducing an energy difference of  $ed_{\text{int}}F_{\perp}$  between the layers, where  $e$  is the elementary charge and  $d_{\text{int}}$  is the distance between the centers of adjacent layers. Correspondingly, the bandgap of 2L WSe<sub>2</sub> becomes spatially indirect, occurring between one layer's conduction band and the other layer's valence band, depending on the direction of the field (Fig. 1b). This interlayer bandgap is approximately  $E_{2\text{L}} = E_{2\text{L}}^0 - ed_{\text{int}}F_{\perp}$ . Therefore, by extracting  $E_{2\text{L}}$  from electrical transport measurements, we can directly determine the field strength. Although this simplified model does not take into account e.g. hybridization between bands or screening, detailed DFT calculations for WSe<sub>2</sub> predict a linear dependence of interlayer bandgap on the interlayer field with  $e^{-1}dE_{2\text{L}}/dF_{\perp} \approx 0.6$  nm<sup>43</sup>, which we use for  $d_{\text{int}}$  in our estimates.

## Device fabrication

A schematic of the dual IL gated FET is shown in Fig. 2a. We choose WSe<sub>2</sub> due to its relatively small bandgap,  $E_{2\text{L}}^0 \approx 1.8$  eV<sup>44–46</sup> and low defect density. We suspend WSe<sub>2</sub> over a  $\sim 10$   $\mu\text{m}^2$  rectangular hole in a silicon nitride (SiN) membrane on a Si substrate. Gold electrodes on top of the SiN electrically contact the 2DM. A separate pair of electrodes on top of the SiN are used as the top gate electrode, which sets the potential of the top IL, and top reference electrode, which measures the potential of the top IL (Fig. 2b). Just before the measurement, a drop of IL (DEME-TFSI<sup>20</sup>) is placed on the back of the Si/SiN chip, which is subsequently placed onto a sapphire chip with gold electrodes serving as bottom gate/reference electrodes. Finally, a drop of IL is deposited onto the device such that it is not in contact with the lower liquid, and the entire assembly is loaded into an electrical probe station where it is measured at room temperature and low pressure,  $\sim 10^{-4}$  mbar (Fig. 2c, see methods and SI for more fabrication and measurement details).

## Extracting $F_{\perp}$ from reference voltage measurements

Our first goal is to establish control of the potential difference between the top and bottom ILs. For this experiment, we use 1L WSe<sub>2</sub> (sample #1). We sweep a potential difference between bottom and top gate electrodes,  $\Delta V = V_{\text{b}} - V_{\text{t}}$ , while recording the potentials of top and bottom

ILs,  $V_t^{\text{ref}}$  and  $V_b^{\text{ref}}$  respectively, as measured by corresponding reference electrodes. The potential dropping across the 2DM,  $\Delta V^{\text{ref}} = V_b^{\text{ref}} - V_t^{\text{ref}}$ , is roughly half of the applied voltage,  $\Delta V$ , and depends on it linearly (Fig. 3). We quantify this linear relationship with gating efficiency,  $\alpha = \Delta V^{\text{ref}}/\Delta V \approx 62\%$  (see SI for details). This linear dependence allows us to avoid using reference electrodes in the devices where transport measurements are performed. Finally, we estimate the electric field strength across the 2DM as  $F_{\perp} = \Delta V^{\text{ref}}/d_{\text{ion}}$ , with  $d_{\text{ion}} \approx 1.8$  nm for 1L WSe<sub>2</sub>. The field estimated in this fashion is shown in Fig. 3. It reaches  $\sim 3$  V/nm near the limit of our electrochemical window, very close to the rough estimate discussed earlier. This measured field surpasses the dielectric strength of common gate dielectrics such as hBN<sup>10,11</sup>, SiO<sub>2</sub><sup>12</sup>, SiN<sup>13,14</sup>, and HfO<sub>2</sub><sup>15</sup>. Nevertheless, even at this field, leakage current remains negligibly small and  $\Delta V^{\text{ref}}$  remains stable.

### Electrical transport and bandgap determination in dual IL-gated monolayer WSe<sub>2</sub>

After estimating a large perpendicular electric field reaching  $\sim 3$  V/nm using reference voltages, we turn to electrical transport measurements of 2DMs to independently confirm the field strength. We start with a simpler test case of monolayer (1L) WSe<sub>2</sub> (sample #2). The bandgap of 1L WSe<sub>2</sub>,  $E_{1L}$ , does not depend on perpendicular field, at least in the first-order approximation<sup>47,48</sup>, making it useful for testing the validity of our approach. To measure the bandgap, we analyze the dependence of drain-source current,  $I_{\text{ds}}$ , through 1L WSe<sub>2</sub> on top and bottom gate voltages individually (Fig. 4a). We observe ambipolar transport with a region of negligibly low current. This region corresponds to the Fermi level ( $E_F$ ) inside the bandgap of the material, while the areas of conductance to the left or right of that region correspond to  $E_F$  within the valence or conduction band respectively<sup>5,9,19,32,49</sup>. The bandgap is calculated from transport measurements (following Ref. <sup>19</sup>) as  $E_{1L} = e\alpha(V_e - V_h)$ , where  $V_e$  and  $V_h$  are conduction and valence band threshold voltages respectively which correspond to the Fermi level at the conduction and valence band extrema. From the measured  $V_e - V_h \approx 3.4$  V and using literature values of  $E_{1L} = 1.9$  eV<sup>19,50,51</sup>, we extract a gating efficiency of  $\alpha \approx 56\%$ . This value is very close to what is obtained from the previous analysis of Fig. 3.

Next, we record a map of  $I_{\text{ds}}$  vs. ( $V_b$ ,  $V_t$ ) for the same sample (Fig. 4b). We assume equal coupling of top and bottom ILs to the material, and therefore the Fermi level of the system is controlled by  $V_g = V_b + V_t$ , whereas the field across the 2DM depends on  $\Delta V = V_b - V_t$ . We observe a clear dependence of  $I_{\text{ds}}$  on  $V_g$  and independence of  $I_{\text{ds}}$  on  $\Delta V$  (other than what appears to be a deviation near  $\Delta V = 0$  V). This  $\Delta V$ -independence is expected because perpendicular electric fields do not significantly affect the bandgap of 1L TMDCs<sup>47,48</sup>. Overall, we confirm that electrical transport measurements can be used to determine the bandgap of our 2DMs, and we observe that the bandgap of 1L WSe<sub>2</sub> does not depend on perpendicular electric field.

### Field strength and bandgap closing in dual IL-gated bilayer WSe<sub>2</sub>

Finally, we turn to the central result of this paper, experimental quantification of perpendicular electric field strength in dual IL-gated FETs. We first record a map of  $I_{ds}$  vs.  $(V_b, V_t)$  for a bilayer (2L) WSe<sub>2</sub> device, sample #3 (Fig. 5a), which looks very different from the monolayer map considered previously (Fig. 4b). We see that the region of zero conductivity (black region) along the  $V_g$  direction gradually shrinks with  $\Delta V$ . In general, this behavior indicates the expected reduction of the bandgap,  $E_{2L}$ , with applied field. In Fig. 5b, we simulate the behavior and plot the regions in which the Fermi level of the suspended part of WSe<sub>2</sub> is inside the bandgap and zero conductivity is expected (black region). We see that this region closely corresponds to the experimentally observed region of no current. However, this sample contains a part of WSe<sub>2</sub> supported on SiN which is in contact with the top IL, but not the bottom IL (Fig. S2 of the SI). The shaded regions in Fig. 5b indicate that the Fermi level of the supported part of the 2DM is inside the conduction or valence bands. Therefore, the current through the 2DM may be strongly distorted or even dominated by the supported part, and we cannot accurately determine the bandgap (and hence  $F_{\perp}$ ) of the suspended part of the 2DM.

To overcome this issue, in sample #4, we covered the supported parts of our 2DM and the drain/source electrodes with a crosslinked chemically-stable organic polymer (PMMA), effectively eliminating the current through the supported part of the 2DM by restricting the region of the 2DM in contact with the top IL (Fig. S2 of the SI). Additionally, in our transport measurements we sweep  $V_g$  and  $\Delta V$  (instead of  $V_b$  and  $V_t$ ) in order to minimize effects of hysteresis (see SI) and to more directly visualize the effects that a varying field and Fermi level have on  $I_{ds}$ . We again observe gradual reduction of the bandgap with  $\Delta V$  (Fig. 5c), which we simulate in Fig. 5d (see Methods for simulation details). The deviation between the data and the simulation is likely due to hysteretic effects that are known to be strong in ILs or slight disparities in top/bottom gating efficiencies (see SI). At large  $\Delta V \approx 5.3$  V, we observe that the bandgap decreases to zero. This behavior signals long-expected field-induced semiconductor-to-metal transition in 2L WSe<sub>2</sub>, predicted to occur near 3 V/nm<sup>37</sup>. In that scenario, the field-induced shift of the conduction band of one layer vs. the valence band of the other layer is large enough for these bands to touch.

To quantify the electric field strength from the map, we first calculate the gating efficiency,  $\alpha \approx 81\%$ , using  $E_{2L} = e\alpha(V_e - V_h)$  along the slice of the map in Fig. 5c where  $\Delta V = 0$  V, because  $E_{2L} = E_{2L}^0 = 1.8$  eV along this slice of the map. Then we use this gating efficiency to calculate the bandgap,  $E_{2L} = e\alpha(V_e - V_h)$ , at each  $\Delta V$ . From that, we calculate the electric field strength through the bilayer,  $F_{\perp}(\Delta V) = (ed_{int})^{-1}[E_{2L}^0 - E_{2L}(\Delta V)]$ . The extracted electric field strength reaches  $\sim 3$  V/nm (Fig. 5e, red), and is in reasonable agreement with our previous measurements from reference voltage data in sample #1 at large  $\Delta V$  (Fig. 5e, gray). The difference in field strengths estimated using different methods could be because of inaccuracies in estimating  $d_{ion}$ , or may be related to the effect of spatially-varying dielectric constant at the nanometer scale neglected in our approach.

It is worth noting one deviation of our experimental data in Figs. 5a from the simulation in Figs. 5b. For the measured data (Fig. 5a), we see a small region of low conductivity at  $\Delta V$  just before apparent bandgap closing (red contour line). The data from sample #4 (Fig. 5c) also shows a region of low conductivity at  $\Delta V$  just after bandgap closing (red contour line). In these regions of low conductivity, the binding energy of interlayer excitons may be larger than the interlayer bandgap, which would result in an interlayer excitonic insulator state<sup>39</sup>. A drop in conductivity may be a signature of the formation of such a state. We should finally mention that even the sample #4 of Fig. 5c may contain regions only in contact with one IL. This is due to a potential misalignment between the hole in the SiN (area of interface with the bottom IL) and the hole in the PMMA mask (area of interface with the top IL). Such a region in contact with a single IL may potentially cause artifacts (including overestimation of the field strength in Fig. 5e) in transport measurements by shunting the suspended part of the flake. While polymer masking discussed earlier mostly addresses this problem, future optical measurements of interlayer exciton energies vs.  $F_{\perp}$  may be used as a reliable alternative method of confirming the field strength.

## Discussion

The field strength estimated from our measurements,  $\sim 3$  V/nm, is the largest static field ever reported through any electronic device, to the best of our knowledge. This field strength should already be sufficient to induce multiple predicted but still unobserved electronic and structural phases in various 2DMs<sup>37,38,40,41</sup>. Furthermore, the maximum field we report is not limited by our technique, but rather by the material we use to record the field strength. The interlayer bandgap of 2L WSe<sub>2</sub> closes at  $F_{\perp} \approx 3$  V/nm, preventing measurements of higher field strengths using transport measurements. The map in Fig. 5c suggests that this limitation is already reached in our device. The use of higher-bandgap 2DMs or an implementation of other field-sensitive phenomena may enable measurements of even larger fields. It is interesting to note that the fields extracted from our measurements are on the same scale or higher compared to the dielectric breakdown strength of 2DMs. While the maximum field in dielectric-based devices are limited by the breakdown of both the gate dielectric as well as of the material under study, in ionic gating approaches the limitation is due to electrochemistry at interfaces. Electrical currents across the IL/2DM interface can only flow when the potential difference across that interface exceeds its electrochemical window (see SI for details about leakage current analysis). When the 2DM is left floating and charge-neutral (as in the experiments of Fig. 3), we expect an enhanced electrochemical window of the IL/2DM/IL system as chemical reactions between the two ILs are suppressed due to an ultrathin barrier (the 2DM) separating them. We finally mention that our device provides the first demonstration of a new type of EDL consisting of IL/2DM/IL instead of the conventional IL/metal electrochemical system. This novel EDL may unlock new areas of research e.g. dielectric breakdown of materials in extreme fields which could lead to enhanced FET gate dielectrics.

## Summary

In conclusion, we developed a new type of FET allowing dual electrochemical gating of 2DMs or other ultrathin films. We demonstrated that our technique can reach electric fields of  $\sim 3$  V/nm inside the FET channel material through a pair of independent measurements: electrochemical reference voltage measurements as well as gate voltage-dependent interlayer bandgap measurements of a bilayer TMDC. To the best of our knowledge, the field we report is the highest static field ever reported for a condensed matter system. Our dual IL-gated design should be compatible with a large variety of 2DMs, other thin films, ILs, and other ionic compounds (such as ionic gels, polymer electrolytes, etc...)<sup>17</sup>, and it allows for simultaneous electrical and optical measurements. We expect that the ability to induce very large fields in condensed matter systems will unlock access to novel predicted but unobserved states of matter, and our results hint at a room-temperature and field-tunable interlayer excitonic insulator state. It is also worth noting that our experimental geometry may allow increasing, by a factor of two, the maximum carrier density achievable in conventional ion-gated FETs with just one gate. Finally, our novel dual IL gate FET design should facilitate exploration of new areas of research requiring ultrahigh carrier densities and/or ultrahigh static electric fields previously experimentally inaccessible in condensed matter systems.

## Methods

### Fabrication details

The devices are fabricated by dry transferring<sup>52</sup> a 2DM (WSe<sub>2</sub>) over a  $\sim 10$   $\mu\text{m}^2$  hole patterned in SiN. Standard electron beam lithography, metal evaporation, and liftoff techniques are used to define source, drain, gate, and reference electrodes (70 nm Au with 3 nm Cr adhesion layer). Finally, the device is covered with PMMA, which is crosslinked over the drain/source electrodes and the 2DM (except for the area over the hole). After removing PMMA, this step results in a mask isolating drain/source electrodes and supported WSe<sub>2</sub> from the top ionic liquid. The sapphire bottom gating chip with similar gate and reference electrodes is produced independently using the same standard techniques described above.

### Simulations

We assume that the bandgap,  $E_{2L}$ , of substrate-supported 2L WSe<sub>2</sub> is constant. The bandgap of suspended 2L WSe<sub>2</sub> depends on the perpendicular field,  $E_{2L} = E_{2L}^0 - ed_{\text{int}}|F_{\perp}|$ , where  $F_{\perp} = \Delta V^{\text{ref}}/d_{\text{ion}} = \alpha\Delta V/d_{\text{ion}}$ . Here,  $\Delta V \equiv V_b - V_t$ ,  $E_{2L}^0 = 1.8$  eV,  $d_{\text{int}} = 0.6$  nm,  $d_{\text{ion}} = 1.4$  nm, and  $\alpha \approx 81\%$  (estimated from Fig. 5c). We assume no built-in doping, so the Fermi level is inside the bandgap when  $-E_{2L}/2 < eV_g < E_{2L}/2$ , where  $V_g \equiv V_b + V_t$  for suspended parts of the 2DM. For supported parts, this criterion is  $-E_{2L}^0/2 < eV_t < E_{2L}^0/2$ .

## Acknowledgments

We gratefully acknowledge Dr. Kyrylo Greben for useful discussions. This work was supported by the Deutsche Forschungsgemeinschaft (DFG)—Projektnummer 182087777—SFB 951 and ERC Starting Grant No. 639739.

### Author contributions

BIW, YH, and JNK fabricated the samples. BIW and YH conducted the measurements. BIW analyzed the data and carried out the simulations. KIB conceived the approach and supervised the project. All authors contributed to writing the manuscript.

### Competing interests

The authors declare no competing interests.

### References

1. Shockley, W. A unipolar “field-effect” transistor\*. *Proc. IRE* **40**, 1365–1376 (1952).
2. Novoselov, K. S. *et al.* Electric field effect in atomically thin carbon films. *Science* (80-. ). **306**, 666–669 (2004).
3. Zibouche, N., Philipsen, P., Kuc, A. & Heine, T. Transition-metal dichalcogenide bilayers: Switching materials for spintronic and valleytronic applications. *Phys. Rev. B - Condens. Matter Mater. Phys.* **90**, 125440 (2014).
4. Guan, H. *et al.* Inversion Symmetry Breaking Induced Valley Hall Effect in Multilayer WSe<sub>2</sub>. *ACS Nano* **13**, 9325–9331 (2019).
5. Zhang, Y. *et al.* Direct observation of a widely tunable bandgap in bilayer graphene. *Nature* **459**, 820–823 (2009).
6. Mak, K. F., Lui, C. H., Shan, J. & Heinz, T. F. Observation of an electric-field-induced band gap in bilayer graphene by infrared spectroscopy. *Phys. Rev. Lett.* **102**, 256405 (2009).
7. Oostinga, J. B., Heersche, H. B., Liu, X., Morpurgo, A. F. & Vandersypen, L. M. K. Gate-induced insulating state in bilayer graphene devices. *Nat. Mater.* **7**, 151–157 (2008).
8. Wang, Z., Chiu, Y.-H., Honz, K., Mak, K. F. & Shan, J. Electrical Tuning of Interlayer Exciton Gases in WSe<sub>2</sub> Bilayers. *Nano Lett.* **18**, 137–143 (2018).
9. Chu, T., Ilatikhameneh, H., Klimeck, G., Rahman, R. & Chen, Z. Electrically Tunable Bandgaps in Bilayer MoS<sub>2</sub>. *Nano Lett.* **15**, 8000–8007 (2015).
10. Hattori, Y., Taniguchi, T., Watanabe, K. & Nagashio, K. Anisotropic Dielectric Breakdown Strength of Single Crystal Hexagonal Boron Nitride. *ACS Appl. Mater. Interfaces* **8**, 27877–27884 (2016).
11. Hattori, Y., Taniguchi, T., Watanabe, K. & Nagashio, K. Layer-by-layer dielectric breakdown of hexagonal boron nitride. *ACS Nano* **9**, 916–921 (2015).
12. Murrell, M. P. *et al.* Spatially resolved electrical measurements of SiO<sub>2</sub> gate oxides using



- atomic force microscopy. *Appl. Phys. Lett.* **62**, 786–788 (1993).
13. Liu, Z. *et al.* Investigation of the interface between LPCVD-SiN<sub>x</sub> gate dielectric and III-nitride for AlGaIn/GaN MIS-HEMTs. *J. Vac. Sci. Technol. B, Nanotechnol. Microelectron. Mater. Process. Meas. Phenom.* **34**, 041202 (2016).
  14. Surana, V. K. *et al.* Realization of high quality silicon nitride deposition at low temperatures. *J. Appl. Phys.* **126**, 115302 (2019).
  15. Han, K. & Zhu, L. GaN MOSHEMT employing HfO<sub>2</sub> as a gate dielectric with partially etched barrier. *Semicond. Sci. Technol.* **32**, 095004 (2017).
  16. Illarionov, Y. Y. *et al.* Insulators for 2D nanoelectronics: the gap to bridge. *Nature Communications* **11**, 1–15 (2020).
  17. Goldman, A. M. Electrostatic Gating of Ultrathin Films. *Annu. Rev. Mater. Res.* **44**, 45–63 (2014).
  18. Xu, K. & Fullerton-Shirey, S. K. Electric-double-layer-gated transistors based on two-dimensional crystals: recent approaches and advances. *J. Phys. Mater.* **3**, 032001 (2020).
  19. Zhang, H., Berthod, C., Berger, H., Giamarchi, T. & Morpurgo, A. F. Band Filling and Cross Quantum Capacitance in Ion-Gated Semiconducting Transition Metal Dichalcogenide Monolayers. *Nano Lett.* **19**, 8836–8845 (2019).
  20. Sato, T., Masuda, G. & Takagi, K. Electrochemical properties of novel ionic liquids for electric double layer capacitor applications. *Electrochim. Acta* **49**, 3603–3611 (2004).
  21. Liu, S. *et al.* In-situ STM and AFM Studies on Electrochemical Interfaces in imidazolium-based ionic liquids. *Electrochim. Acta* **309**, 11–17 (2019).
  22. S Barbosa, M., Balke, N., Tsai, W. Y., Santato, C. & Orlandi, M. O. Structure of the Electrical Double Layer at the Interface between an Ionic Liquid and Tungsten Oxide in Ion-Gated Transistors. *J. Phys. Chem. Lett.* **11**, 3257–3262 (2020).
  23. Hayes, R. *et al.* Double Layer Structure of Ionic Liquids at the Au(111) Electrode Interface: An Atomic Force Microscopy Investigation. *J. Phys. Chem. C* **115**, 6855–6863 (2011).
  24. Black, J. M. *et al.* Fundamental aspects of electric double layer force-distance measurements at liquid-solid interfaces using atomic force microscopy. *Sci. Rep.* **6**, 1–12 (2016).
  25. Rodenbücher, C., Wippermann, K. & Korte, C. Atomic Force Spectroscopy on Ionic Liquids. *Appl. Sci.* **9**, 2207 (2019).
  26. Baldelli, S. Surface structure at the ionic liquid-electrified metal interface. *Accounts of Chemical Research* **41**, 421–431 (2008).
  27. Ye, J. *et al.* Accessing the transport properties of graphene and its multilayers at high carrier density. *Proc. Natl. Acad. Sci. U. S. A.* **108**, 13002–13006 (2011).

28. Zhao, S. *et al.* Quantitative Determination on Ionic-Liquid-Gating Control of Interfacial Magnetism. *Adv. Mater.* **29**, 1606478 (2017).
29. Ye, J. T. *et al.* Superconducting dome in a gate-tuned band insulator. *Science (80-. )*. **338**, 1193–1196 (2012).
30. Shi, W. *et al.* Superconductivity Series in Transition Metal Dichalcogenides by Ionic Gating. *Sci. Rep.* **5**, 12534 (2015).
31. Zakhidov, D., Rehn, D. A., Reed, E. J. & Salleo, A. Reversible Electrochemical Phase Change in Monolayer to Bulk-like MoTe<sub>2</sub> by Ionic Liquid Gating. *ACS Nano* **14**, 2894–2903 (2020).
32. Zheng, L. M. *et al.* Ambipolar ferromagnetism by electrostatic doping of a manganite. *Nat. Commun.* **9**, (2018).
33. Chu, L. *et al.* Charge transport in ion-gated mono-, bi-, and trilayer MoS<sub>2</sub> field effect transistors. *Sci. Rep.* **4**, 1–6 (2014).
34. Jeon, D. Y. *et al.* Tuning the on/off current ratio in ionic-liquid gated multi-layer MoS<sub>2</sub> field-effect transistors. *J. Phys. D. Appl. Phys.* **53**, 275104 (2020).
35. Chen, Q. *et al.* Continuous Low-Bias Switching of Superconductivity in a MoS<sub>2</sub> Transistor. *Adv. Mater.* **30**, 1800399 (2018).
36. Wang, F. *et al.* Ionic Liquid Gating of Suspended MoS<sub>2</sub> Field Effect Transistor Devices. *Nano Lett.* **15**, 5284–5288 (2015).
37. Ramasubramaniam, A., Naveh, D. & Towe, E. Tunable band gaps in bilayer transition-metal dichalcogenides. *Phys. Rev. B - Condens. Matter Mater. Phys.* **84**, 205325 (2011).
38. Azhikodan, D., Nautiyal, T., Shallcross, S. & Sharma, S. An anomalous interlayer exciton in MoS<sub>2</sub>. *Sci. Rep.* **6**, 37075 (2016).
39. Jérôme, D., Rice, T. M. & Kohn, W. Excitonic insulator. *Phys. Rev.* **158**, 462–475 (1967).
40. Liu, Q., Zhang, X., Abdalla, L. B., Fazzio, A. & Zunger, A. Switching a normal insulator into a topological insulator via electric field with application to phosphorene. *Nano Lett.* **15**, 1222–1228 (2015).
41. Das, B., Sen, D. & Mahapatra, S. Tuneable quantum spin Hall states in confined 1T' transition metal dichalcogenides. *Sci. Rep.* **10**, 1–13 (2020).
42. Wang, J. *et al.* Electric Field-Tunable Structural Phase Transitions in Monolayer Tellurium. *ACS Omega* **5**, 18213–18217 (2020).
43. Dai, X., Li, W., Wang, T., Wang, X. & Zhai, C. Bandstructure modulation of two-dimensional WSe<sub>2</sub> by electric field. *J. Appl. Phys.* **117**, 084310 (2015).
44. Zhang, C. *et al.* Visualizing band offsets and edge states in bilayer-monolayer transition metal dichalcogenides lateral heterojunction. *Nat. Commun.* **6**, 1–6 (2016).

45. Liu, H. J. *et al.* Molecular-beam epitaxy of monolayer and bilayer WSe<sub>2</sub>: A scanning tunneling microscopy/spectroscopy study and deduction of exciton binding energy. *2D Mater.* **2**, 034004 (2015).
46. Yue, R. *et al.* Nucleation and growth of WSe<sub>2</sub>: enabling large grain transition metal dichalcogenides. *2D Mater.* **4**, 045019 (2017).
47. Verzhbitskiy, I., Vella, D., Watanabe, K., Taniguchi, T. & Eda, G. Suppressed Out-of-Plane Polarizability of Free Excitons in Monolayer WSe<sub>2</sub>. *ACS Nano* **13**, 3218–3224 (2019).
48. Zibouche, N., Philipsen, P., Heine, T. & Kuc, A. Electron transport in MoWSeS monolayers in the presence of an external electric field. *Phys. Chem. Chem. Phys.* **16**, 11251–11255 (2014).
49. Mitta, S. B. *et al.* Electrical characterization of 2D materials-based field-effect transistors. *2D Materials* **8**, 012002 (2021).
50. Park, S. *et al.* Direct determination of monolayer MoS<sub>2</sub> and WSe<sub>2</sub> exciton binding energies on insulating and metallic substrates. *2D Mater.* **5**, 025003 (2018).
51. Zhang, C. *et al.* Probing Critical Point Energies of Transition Metal Dichalcogenides: Surprising Indirect Gap of Single Layer WSe<sub>2</sub>. *Nano Lett.* **15**, 6494–6500 (2015).
52. Castellanos-Gomez, A. *et al.* Deterministic transfer of two-dimensional materials by all-dry viscoelastic stamping. *2D Mater.* **1**, 011002 (2014).

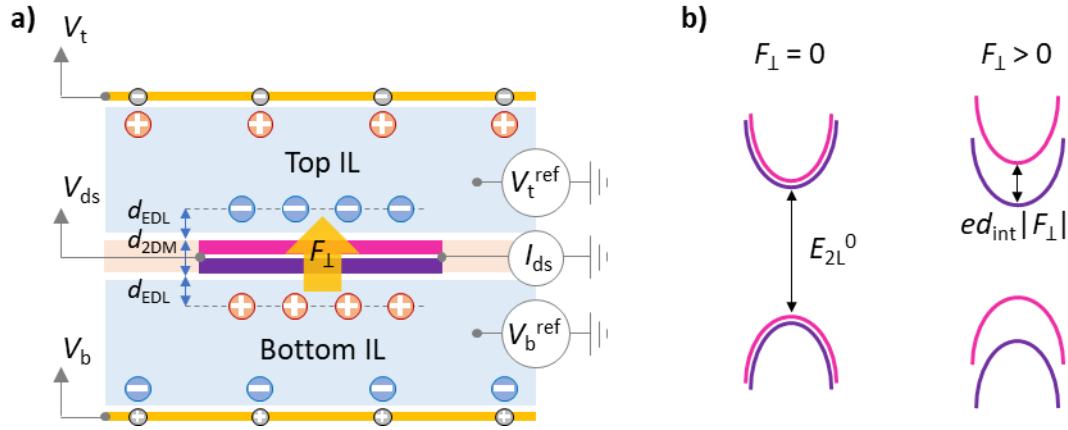


**Fig. 1 | Dual ionic liquid gating.** **a)** Concept of the dual ionic liquid-gated bilayer TMDC device. The potentials of the top and the bottom ionic liquids are independently controlled by top and bottom gate voltages,  $V_t$  and  $V_b$  respectively. The potential difference between top and bottom ionic liquids drops over a  $\sim 1$  nm thick layer (including the 2DM), thereby generating an ultrastrong electric field through it. **b)** A band structure sketch of a bilayer TMDC at zero and non-zero electric field. The field breaks the degeneracy between the energy bands localized at top and at the bottom TMDC layers and reduces the interlayer bandgap by  $ed_{int}|F_{\perp}|$ .

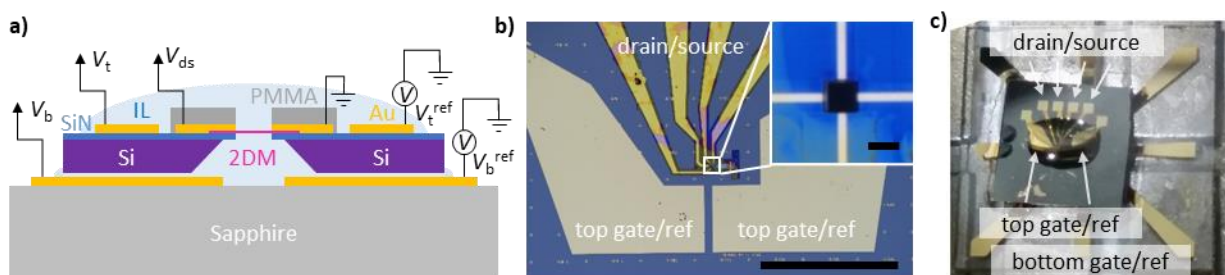


**Fig. 2 | Device and measurement overview.** **a)** Side-view cartoon of the device and measurement scheme. **b)** Microscope (5x) image of sample #2 before applying ionic liquids. Drain and source electrodes are covered with crosslinked PMMA. Scale bar is 1 mm. **Inset:** 100x image of the TMDC deposited onto a square hole ( $\sim 3 \mu\text{m} \times 3 \mu\text{m}$ ) in SiN. Everything in the inset other than the area of TMDC over the hole is covered by crosslinked PMMA. Scale bar is  $3 \mu\text{m}$ . **c)** Photograph of sample #2 just before measurement (SiN chip is 5 mm x 5 mm). Notice: the top and bottom ionic liquids are not in contact.

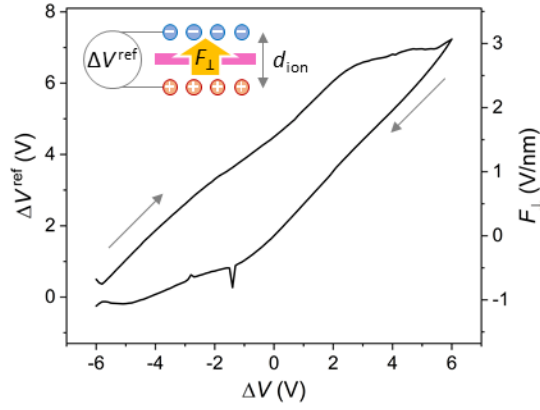


**Fig. 3 | Estimating the perpendicular field from electrochemical measurements.** Difference between top and bottom reference voltages,  $\Delta V^{\text{ref}}$ , as well as perpendicular electric field strength,  $F_{\perp}$ , calculated from it as a function of the difference between top and bottom gate potentials,  $\Delta V$ . To convert  $\Delta V^{\text{ref}}$  into electric field,  $F_{\perp}$ , it was first manually shifted to account for a constant offset of  $\Delta V^{\text{ref}}$  for that device, likely caused by contamination on the electrode's surface, ensuring that  $F_{\perp}$  is zero when  $\Delta V = 0$  V along the more linear downward sweep.

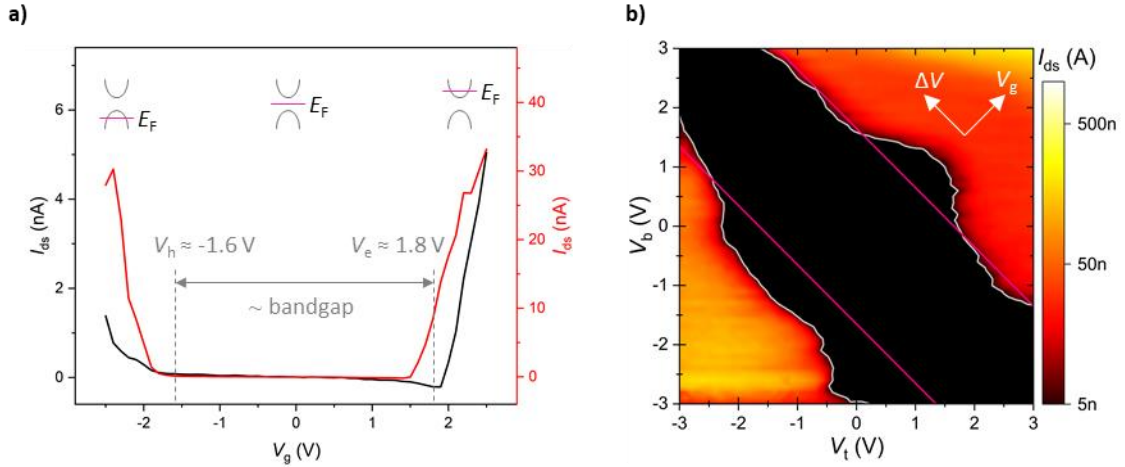


**Fig. 4 | Transport measurements for monolayer WSe<sub>2</sub>.** **a)** Current across 1L WSe<sub>2</sub> sample #2 as a function of the bottom gate voltage with top gate set to zero (black curve) and as a function of the top gate voltage with bottom gate set to zero (red curve). The region of near-zero current ( $I_{ds} < 100$  pA) seen in both curves corresponds to the Fermi level,  $E_F$ , located inside the bandgap of the material. The cartoons indicate the Fermi level positions as a function of  $V_g$ . **b)** Map of  $I_{ds}$  vs. ( $V_b$ ,  $V_t$ ) for the same device. The white contours indicate the valence and conduction band threshold voltages from the measurement and the pink lines indicate the simulation results for valence and conduction band threshold voltages.

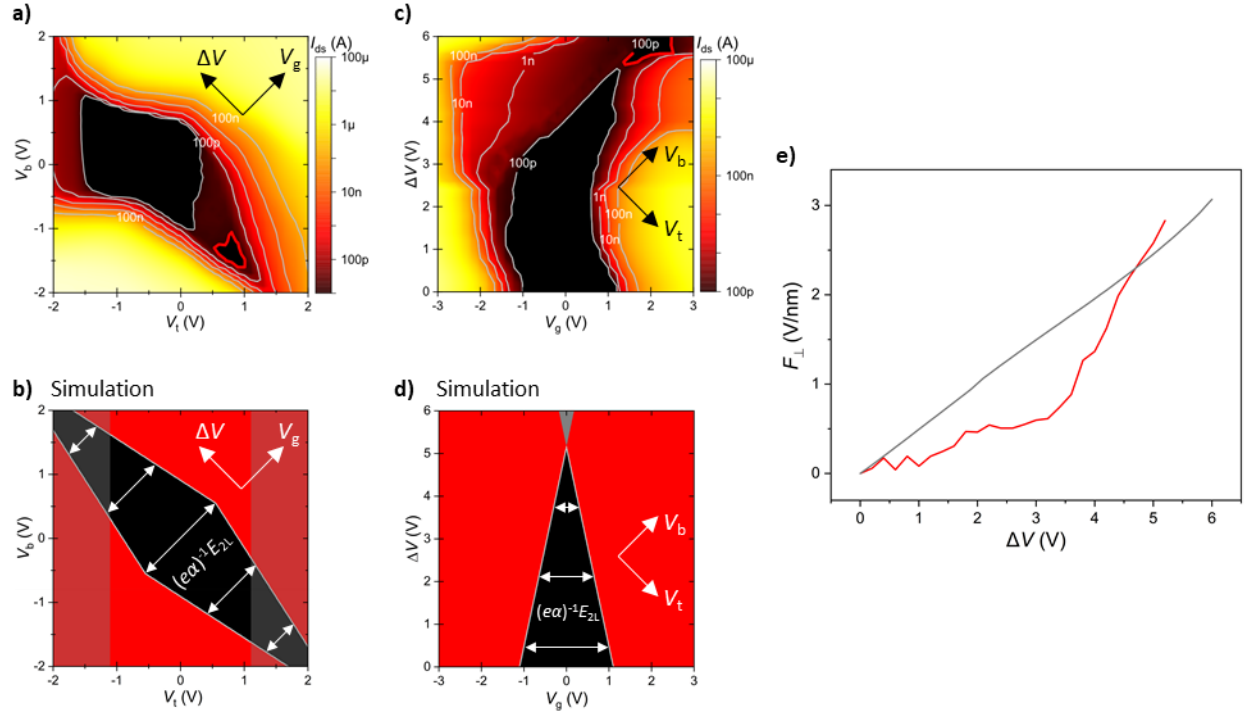


**Fig. 5 | Field strength measurement from transport in bilayer WSe<sub>2</sub>.** **a)** Map of  $I_{ds}$  vs.  $(V_b, V_t)$  for 2L WSe<sub>2</sub> device (sample #3). **b)** Simulated conductivity for the same sample. The Fermi level is inside the bandgap of the suspended part of the 2DM inside the black region, and conductivity is expected to be low. Inside shaded regions, the current may be dominated by the supported part of the 2DM. **c)** Map of  $I_{ds}$  vs.  $(\Delta V, V_g)$  for 2L WSe<sub>2</sub> device (sample #4) in which the entire flake outside of the suspended region is covered by crosslinked polymer. **d)** Simulated conductivity of the same sample. **e)** Perpendicular electric field,  $F_{\perp}$ , obtained from the measured bandgap  $E_{2L}$  vs.  $\Delta V$  of sample #4 (red curve). The perpendicular electric field obtained from reference voltage measurements of Fig. 3 is shown as the gray curve for comparison.



## Supplementary information

### Sample fabrication

Fig. S1 shows images of all samples used in the main text at various stages of the fabrication process. Silicon nitride (SiN) membranes were purchased from Norcada (20 nm SiN on Si). A  $\sim 3 \mu\text{m} \times 3 \mu\text{m}$  hole in the SiN membrane was created using focused ion beam lithography. Flakes of 2D materials (2DMs) were mechanically exfoliated onto a thin piece of PDMS purchased from GelPak ( $\sim 6$  mils thick, X4 retention factor) using the standard “scotch tape” technique<sup>1</sup>. The flakes were subsequently dry transferred<sup>2</sup> over the hole in the SiN membrane at  $60^\circ\text{C}$  using a homemade transfer system. We fabricate electrodes using standard electron beam lithography (EBL), thermal evaporation (3 nm Cr and 70 nm Au), and liftoff ( $60^\circ\text{C}$  acetone for 1 – 3 hours). Following liftoff, we confirm that the suspended region of the 2DM is not ruptured ( $\sim 25\%$  success rate). Fabrication for sample #3 in the main text ends here.

As a final step for samples #1, #2, and #4, we cover non-suspended regions of the 2DM and the metal electrodes with a layer of cross-linked poly(methyl methacrylate) (PMMA) EBL resist. This capping layer serves several functions (see Fig. S2): 1) it restricts the FET channel area for the top IL to match the channel area for the bottom IL (just the suspended region), thereby eliminating the conductivity contribution from supported regions of the 2DM, 2) it clamps the 2DM at its edges, thereby preventing intercalation of ions in the IL to go between the layers of the 2DM, and 3) it reduces the influence of the drain/source metal electrodes on the total perpendicular capacitance. To fabricate this capping layer, we spin a layer of PMMA and a layer of conductive polymer (Electra 92 from Allresist) after the electrode fabrication step. We then perform EBL for the PMMA crosslinking step to cover the 2DM’s supported region and drain/source electrodes. For our crosslink step, we use a dose of  $10,500 \mu\text{C}/\text{cm}^2$  at 30 kV near the suspended 2DM, and to cover the drain/source electrodes away from the 2DM we use a dose of  $17,500 \mu\text{C}/\text{cm}^2$  at 10 kV. Lastly, we remove the excess unexposed PMMA in heated ( $60^\circ\text{C}$ ) acetone for 3 hours. Fabrication for samples #2 and #4 in the main text ends here. To fabricate sample #1 from the main text, we performed this crosslinking step in a  $1 \text{ mm} \times 1 \text{ mm}$  area around the 2DM immediately following the dry transfer step, and then removed the excess PMMA in the same way as described above.

### Testing crosslinked PMMA capping layer

In our dual IL-gated FETs *without any capping layer* above the 2DM, current may flow through the suspended region of interest as well as supported regions of the flake,  $I_{\text{susp}}$  and  $I_{\text{supp}}$  respectively. We model this as a parallel connection of two different gate-tunable resistors, one resistor modeling the suspended dual-gated region of the 2DM (Fermi level depends on  $V_b + V_t$ ), and the other resistor models the SiN-supported region of the 2DM (Fermi level depends on just  $V_t$ ). The total drain-source current is  $I_{\text{ds}} = I_{\text{susp}} + I_{\text{supp}}$ .

We performed simple test measurements in order to confirm the PMMA capping layer's ability to neutralize the contribution of  $I_{\text{supp}}$  (see Fig. S2). We fabricated a simple 2L WSe<sub>2</sub> device using the same fabrication methods outlined above, but on a different substrate (300 nm SiO<sub>2</sub> thermally grown on Si). The device has two channel regions, one without PMMA (Ch1) and one covered by crosslinked PMMA (Ch2). We apply a drop of DEME-TFSI on top of the center of the WSe<sub>2</sub>, and perform transport measurements of Ch1 and Ch2 simultaneously (see Fig. S2). It is clear from the data that crosslinked PMMA blocks ions from changing the carrier density in the covered region, Ch2, and given the charge-neutrality of the WSe<sub>2</sub>, we see that no current flows through the covered channel.

### Gating efficiency

Our 2DM is exposed to two individual ILs, one above and one below the 2DM. Only a fraction of the potential applied to the gate electrodes ( $V_b$ ,  $V_t$ ) inside these liquids falls across the 2DM/IL interface ( $V_b^{\text{ref}}$ ,  $V_t^{\text{ref}}$ ), which is characterized by gating efficiencies:  $\alpha_b \equiv V_b^{\text{ref}}/V_b$  and  $\alpha_t \equiv V_t^{\text{ref}}/V_t$ . These gating efficiencies depend on the type of electrolyte and the size of the gate electrodes (relative to the 2DM and exposed drain/source electrodes). In our devices, we try to equalize these parameters between top and bottom gate electrodes. The size, material composition, and placement of the gate electrodes above and below the 2DM are roughly equal. Because of this symmetry between top and bottom gate electrodes, we assume  $\alpha_b = \alpha_t = \alpha$ . Similarly, we can relate ( $V_g$ ,  $\Delta V$ ) to the fraction of those applied voltages, ( $V_g^{\text{ref}}$ ,  $\Delta V^{\text{ref}}$ ), and when we assume  $\alpha_b = \alpha_t = \alpha$ , we see that  $\alpha = V_g^{\text{ref}}/V_g = \Delta V^{\text{ref}}/\Delta V$ . Therefore, everywhere in the main text, we just use a single parameter,  $\alpha$ , without specifying which gate it refers to.

To extract  $\alpha$  from the data of Fig. 3, the  $\Delta V^{\text{ref}}$  vs  $\Delta V$  data (sample #1, 1L WSe<sub>2</sub>) of the main text was linearly fitted averaging up and down sweep directions. From the slope of the fit, we obtain  $\alpha \approx 62\%$  in this device. We also see in Fig. S3b that the voltage drop across both gate EDLs as a function of  $\Delta V$  are almost the same, confirming that  $\alpha_b \approx \alpha_t$  in this device. Comparing this with  $\alpha \approx 56\%$  obtained from transport measurements in a different device (sample #2, also 1L WSe<sub>2</sub>) further confirms our assumption that  $\alpha_b \approx \alpha_t$  in our experiments.

From the 2L WSe<sub>2</sub> data in Fig. 5c, we can calculate an average value of  $d_{\text{ion}}$  using the determined gating efficiency for this device,  $\alpha \approx 81\%$ , and the value of  $\Delta V$  and  $F_{\perp}$  at bandgap closing, 5.3 V and 3 V/nm respectively. We calculate  $d_{\text{ion}} = \alpha * \Delta V / F_{\perp} \approx 1.4$  nm. This implies that our estimated value of  $d_{\text{ion}} = 1.8$  nm for 1L WSe<sub>2</sub> in Fig. 3 is probably too high, which means that our calculated  $F_{\perp}$  in Fig. 3 of the main text is likely a lower-bound.

### Electrical measurement

The data in Fig. 3 of the main text was collected by applying a potential difference,  $\Delta V$ , directly between top and bottom gate electrodes and measuring the reference voltage of each ionic liquid (IL) with the 2DM electrically floating. Reference voltages were recorded by sourcing exactly 0 A to the reference electrodes while recording their potential (Keithley 2450). The data in Figs. 4 and 5 used top and bottom gate voltages controlled by separate sourcemeters along

with a third sourcemeter to apply a drain/source potential,  $V_{ds}$  (100 mV for Fig. 4 and Fig. 5c, 50 mV for Fig. 5a).

When taking map data, we swept two gate voltages (Keithley 2450s) in two different coordinate systems:  $(V_b, V_t)$  and  $(V_g, \Delta V)$ . We found that hysteresis is minimized in the latter system, since in that case, both sourcemeters are swept in unison in order to directly control physically relevant quantities, the Fermi level ( $E_F$ ) and the perpendicular electric field ( $F_\perp$ ). When we take map data, the slow axis has negligible hysteresis. Therefore, when we sweep in  $(V_g, \Delta V)$ , we probe the Fermi level ( $E_F$  controlled by  $V_g$ , fast axis) of a relatively constant band structure ( $F_\perp$  controlled by  $\Delta V$ , slow axis). Furthermore, any hysteretic effects in  $V_g$  should not affect our bandgap ( $E_{bg}$ ) measurement, because any hysteretic effect,  $V_{hyst}$ , should shift both measured electron and hole threshold voltages roughly equally,  $V_e^{meas} - V_h^{meas} \approx (V_e + V_{hyst}) - (V_h + V_{hyst}) = V_e - V_h = (e\alpha)^{-1}E_{bg}$ .

### Leakage current in our IL-gated devices

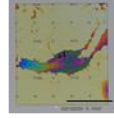
It is important to ensure that  $I_{ds}$  in our devices is separated from the leakage current across our 2DM/IL interface. Below, we show an approach to analyze the leakage current. We model our system as a combination of several capacitors (Fig. S4):  $C_b^w$  and  $C_t^w$  are working electrode capacitors corresponding to the interface between bottom and top gate electrodes and ILs respectively. The counter electrode capacitors,  $C_b^c$  and  $C_t^c$ , model the IL/2DM interface for bottom and top ILs respectively. Finally,  $C_\perp$  models the direct coupling between bottom and top ILs, which couple through both the 2DM and the PMMA/SiN. We model leakage by introducing currents  $I_b^w$ ,  $I_t^w$ ,  $I_b^c$ ,  $I_t^c$ , and  $I_\perp$ , each associated with their respective capacitor. These currents arise due to i) charging/discharging of the corresponding EDLs, or ii) charge transfer due to electrochemical reactions at the corresponding interface<sup>3</sup>. We note that when the 2DM is electrically floating, the 2DM acts as an ideal atomically thin barrier separating the two ILs. This barrier prevents electrochemical reactions between the two ILs while still enabling the study of the interaction between the two ILs when separated by an ultrathin charge-neutral membrane. Due to the expected suppression of electrochemical reactions in this state, we predict that our device geometry will provide a robust platform to study previously-inaccessible phenomena such as dielectric breakdown of the barrier material (without influence of damage from gate leakage currents) and interactions between ions at ultralow distances.

In this model,  $I_b^w$  and  $I_t^w$  are the currents experimentally detected by our sourcemeters applying the corresponding gate voltages. The currents  $I_b^c$  and  $I_t^c$  are the leakage currents flowing in the 2DM and potentially contributing to the measured drain-source current. By invoking Kirchhoff's current law for the circuit in Fig. S4, we get  $I_b^w + I_t^w = I_b^c + I_t^c$ . This means that we can determine the maximum amount of leakage current which could affect our measured  $I_{ds}$  by simply taking the sum of leakage currents detected by the sourcemeters. In Fig. S5, we re-analyzed the current maps shown in Fig. 5a,c by subtracting leakage current determined in this fashion from the measured  $I_{ds}$ . We see that the overall behavior remains unchanged: we observe a gradually shrinking bandgap region as well as the point of band

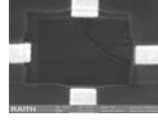
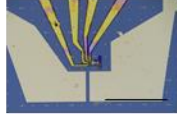
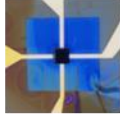
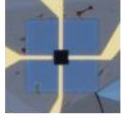
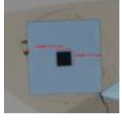
closing. Interestingly, after taking the leakage of Fig. 5c into account, we see that there is a region of low conductance just before bandgap closing similar to Fig. 5a, a feature which is not observed in this data seen in the main text. This region of the map corresponds to the high-field regime just before bandgap closing where an interlayer excitonic insulator is expected, just as in Fig. 5a.

## References

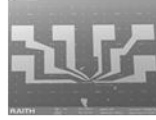
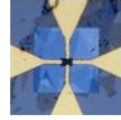
1. Novoselov, K. S. *et al.* Electric field effect in atomically thin carbon films. *Science* (80-. ). **306**, 666–669 (2004).
2. Castellanos-Gomez, A. *et al.* Deterministic transfer of two-dimensional materials by all-dry viscoelastic stamping. *2D Mater.* **1**, 011002 (2014).
3. Xu, K. & Fullerton-Shirey, S. K. Electric-double-layer-gated transistors based on two-dimensional crystals: recent approaches and advances. *J. Phys. Mater.* **3**, 032001 (2020).



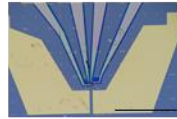
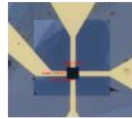
**a)** Sample 1: 1L WSe<sub>2</sub> w/PMMA no electrodes



**b)** Sample 2: 1L WSe<sub>2</sub> w/PMMA



**c)** Sample 3: 2L WSe<sub>2</sub> w/out PMMA



**d)** Sample 4: 2L WSe<sub>2</sub> w/PMMA

**Fig. S1 | Samples from the main text. a)** Sample #1 after transfer (100x) and crosslinking (100x and 5x, scale bar in 5x is ~500  $\mu$ m). The sample has no electrodes. **b)** Sample #2 after transfer (100x), metallization (100x), crosslinking (100x and 5x, scale bar in 5x is ~1 mm), and measurement (SEM images). This sample is shown in Fig. 2b,c in the main text. **c)** Sample #3 after transfer (100x), metallization (100x), and measurements (SEM images). SEM images after measurement show no damage to the suspended 2DM, it remains intact and not ruptured. **d)** Sample #4 after transfer (100x), metallization (100x), and crosslinking (100x and 5x).

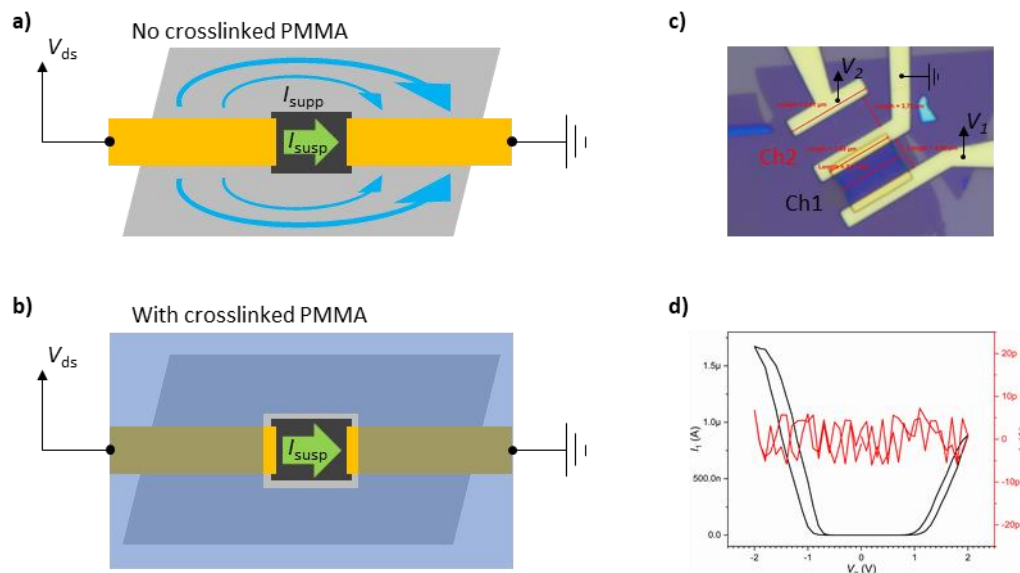


**Fig. S2 | Supported/suspended current and the need for a capping layer.** **a)** and **b)** show how supported current is restricted and minimized with the addition of a PMMA capping layer. **c)** 100x image (with dimensions) showing WSe<sub>2</sub> with two channel areas, uncovered (Ch1) and covered (Ch2) with crosslinked PMMA. **d)** Electrical transport through both channel regions. It is clear from the data that crosslinked PMMA blocks ions from changing the carrier density in covered regions, ensuring that no current will flow in these regions (given that the 2DM is natively charge-neutral).

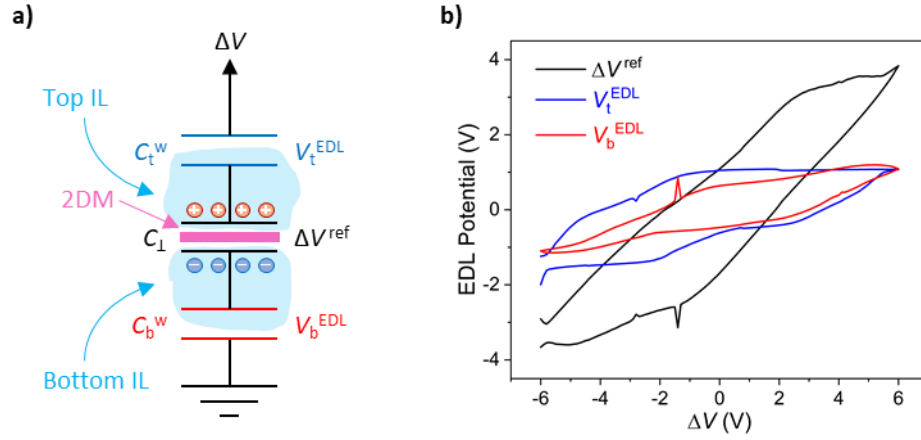


**Fig. S3 | Circuit analysis for Fig. 3.** **a)** The circuit for the reference voltage experiment in Fig. 3 of the main text (see Fig. S4 for complete circuit). **b)** Average voltage drop across the corresponding EDLs as a function of  $\Delta V$  for each of the three capacitors involved (each curve vertically shifted to be centered about the origin). Note that the two gate EDLs have roughly the same value as a function of  $\Delta V$ , thereby confirming that  $\alpha_b \approx \alpha_t$ .

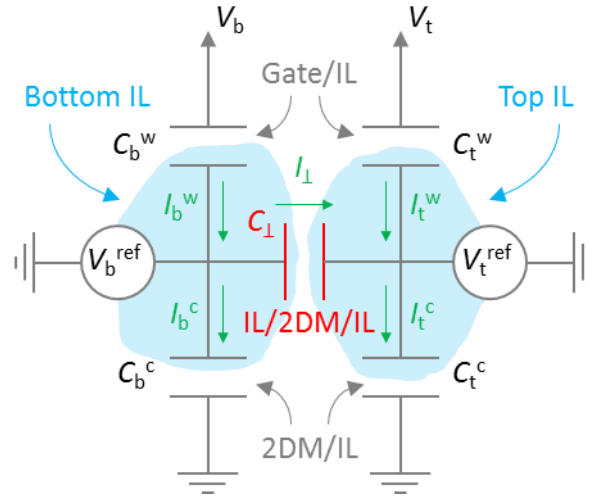


**Fig. S4 | Dual-IL-gated FET gating circuit.** Dual-IL-gating circuit diagram. Each individual IL has its own working (gate) electrode and its own reference voltage. When the 2DM is left floating (circuit in Fig. S3a), the bottom and top counter electrodes,  $C_b^c$  and  $C_t^c$  respectively, are left floating, and therefore do not affect the circuit behavior, as in the case of the reference voltage measurements using sample #1 in Fig. 3 of the main text. The leakage current potentially flowing through the device is the sum of the two counter electrode currents, which is found from the figure using Kirchhoff's current laws and summing the two measured currents from our sourcemeter:  $I_b^w + I_t^w = I_b^c + I_t^c$ .



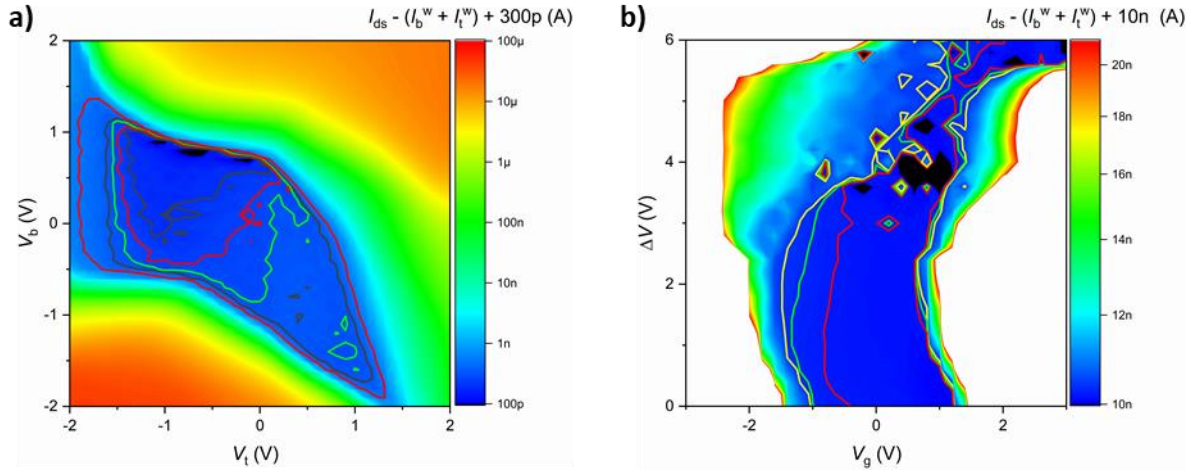


**Fig. S5 | Leakage analysis for transport maps in Fig. 5.** **a)** and **b)** correspond to the transport maps in Figs. 5a and 5c respectively when we subtract the corresponding  $I_b^w + I_t^w$  data. The  $I_{ds} - (I_b^w + I_t^w)$  data may be negative; in which case we add a small flat amount of current to the data in order to make using a log scale meaningful. In both maps, the bandgap closing phenomena is preserved even after subtracting the leakage, indicating that the low current we use in the main text for our threshold voltages correctly models transistor conduction.